RSC Advances

PAPER

View Article Online
View Journal | View Issue

Cite this: *RSC Adv.*, 2019, **9**, 34804

Facile synthesis of a novel WO_3/Ag_2MoO_4 particles-on-plate staggered type II heterojunction with improved visible-light photocatalytic activity in removing environmental pollutants†

Huanli Wang, *[ab] Yafei Wang,[a] Ailing Xu,[a] Qipeng Yang,[a] Fujun Tao,[c] Mingliang Ma,[d] Zhiwen Song*[a] and Xiaobo Chen *[b]

Received 7th September 2019
Accepted 18th October 2019

DOI: 10.1039/c9ra07175j

rsc.li/rsc-advances

A novel WO_3/Ag_2MoO_4 heterojunction has been synthesized through a facile precipitation method with Ag_2MoO_4 particles firmly deposited on the surface of WO_3 nanoplates, forming "particles-on-plate" type II heterojunction structures. This heterojunction exhibited improved photocatalytic activities for the degradation of rhodamine B (RhB), 4 chlorophenol (4-CP) and tetracycline hydrochloride (TC) under visible-light irradiation compared to pure Ag_2MoO_4 and WO_3. In addition, the heterojunction with 10 wt% Ag_2MoO_4 displays the best photocatalytic performance, which was about 2 times better than that of pure WO_3 or Ag_2MoO_4. The TC photodegradation rate reaches up to 91% within 90 min visible light irradiation. Furthermore, the photocatalytic efficiency of the Ag_2MoO_4/WO_3 heterojunction is 1.3 times higher than that of the mixture of the two individual photocatalysts. This remarkable enhanced photocatalytic performance results from the staggered bandgap between Ag_2MoO_4 and WO_3, which can suppress the recombination of electron–hole pairs efficiently. Moreover, based on the radical trapping experiment, the superoxide radical anions (·OH) and photogenerated holes (h^+) are the crucial active oxidizing species.

1. Introduction

Photocatalysis has aroused significant attention recently due to its efficiency, environmental friendliness and convenience for solving the energy and environment crisis. The key to photocatalysis is to construct an efficient and stable photocatalyst.[1,2] To date, various kinds of photocatalysts have been reported such as TiO_2,[3,4] Ag_3PO_4,[5–7] Bi_2WO_6,[8–11] MoS_2,[12,13] C_3N_4,[14,15] $BiVO_4$ (ref. 16) and WO_3.[17–19] Among them, WO_3 is regarded as a promising photocatalyst due to its strong adsorption in visible light, photocorrosion resistance, and stable physicochemical properties. Nevertheless, its practical application is largely restricted due to its comparatively narrow band gap (2.4 to 2.8 eV) and lower light energy conversion efficiency.[20] The commonly used strategies to improve the photocatalytic performance include ion doping,[21] heterojunctions,[22–25] and morphological modulation.[10,26] Among those strategies, the heterojunction is proven to be most widely used because of its effectiveness and convenience for improving the photocatalytic activity, as highlighted in our recent review.[22] Furthermore, we have also constructed some nanojunction systems such as Bi_2O_3–Bi_2WO_6 (ref. 11) and Ag_3PO_4–GQDs composites;[7] these heterojunction photocatalysts exhibited higher photocatalytic activity than their bare components. Therefore, constructing WO_3 based heterojunction photocatalyst should be an effective way to improve the photocatalytic performance of WO_3. Up to date, various WO_3-based heterojunctions have been reported, such as $WO_3/BiVO_4$,[18] WO_3–C_3N_4,[27,28] WO_3/CdS,[29] WO_3/Ag,[30] WO_3/RGO[31] and CNTs–WO_3.[32] Compared with bare WO_3, the construction of these heterojunctions enhanced the photocatalytic performance in different degrees. However, it is still highly desirable to design novel WO_3-based heterojunctions to further improve the photocatalytic performance of pure WO_3. Over the last decade, silver molybdate (Ag_2MoO_4) has attracted extensive attentions in photoluminescence,[33] biological sterilization[34] and electrocatalytic oxygen reduction reaction,[35] and it has been shown as an excellent semiconductor to modify other semiconductors to improve their photocatalytic performance,[36–38] such as $Ag/AgCl/Ag_2MoO_4$,[39] $Ag@Ag_2MoO_4$–AgBr composite,[40,41] Ag_2MoO_4–Ag_3PO_4.[42] As the band edges of Ag_2MoO_4 match well with those of WO_3, it can be expected that the WO_3/Ag_2MoO_4 heterojunction would be a photocatalyst with a staggered bandgap and therefore exhibit a high performance.

[a]School of Environmental and Municipal Engineering, Qingdao University of Technology, China. E-mail: whl_r@126.com; songzhiwen@qut.edu.cn
[b]University of Missouri, USA. E-mail: chenxiaobo@umkc.edu
[c]Shanghai Maritime University, China
[d]School of Civil Engineering, Qingdao University of Technology, China

† Electronic supplementary information (ESI) available. See DOI: 10.1039/c9ra07175j

Also, it is desirable to construct such heterojunction, as it has never been done so far.

In this study, Ag_2MoO_4–WO_3 heterojunctions with various Ag_2MoO_4 mass percentages have been developed with a facile precipitation method. Their photocatalytic activities have been investigated with the photodegradation of rhodamine B (RhB), 4 chlorophenol (4-CP) and tetracycline hydrochloride (TC) under visible-light irradiation. And the mechanism of the improved photocatalytic performance of the heterojunction photocatalysts has also been proposed based on the characterization and analysis results.

2. Experimental

2.1. Chemicals

Degussa TiO_2 with particle size 25 nm (P25), TC and 4-CP were purchased from Shanghai Macklin Biochemical Co., Ltd. $Na_2MoO_4 \cdot 2H_2O$, $Na_2WO_4 \cdot 2H_2O$, $AgNO_3$, HCl, ethanol were purchased from Sinopharm Chemical Reagent Co., Ltd.

2.2. Preparation of tungsten oxide (WO_3) nanoplates

WO_3 nanoplates were synthesized according to ref. 31. In a typical synthesis, $Na_2WO_4 \cdot 2H_2O$ (200 mg) were dissolved in deionized water (10 mL). Subsequently, 5 mL HCl (35%) was slowly added to the above solution with continuous stirring. The suspension was then transferred to a 45 mL Teflon-lined stainless-steel autoclave and heated at 140 °C for 8 h. The sample was collected by centrifugation with ethanol and deionized water for several times and dried by vacuum freeze drier. Finally, the samples obtained were annealed at 300 °C for 30 min.

2.3. Preparation of silver molybdate (Ag_2MoO_4) and Ag_2MoO_4–WO_3

The surface decoration of WO_3 with Ag_2MoO_4 nanoparticles (NPs) was accomplished by a simple *in situ* deposition method. Briefly, a certain amount of WO_3 (0.375, 0.75, 1.125 and 1.5 g) was dispersed into 40 ml deionized water and sonicated for 30 min to give a WO_3 aqueous suspension. Then, $AgNO_3$ (5 mM, 40 mL) was dissolved in the above suspension under constant stirring. After that, $Na_2MoO_4 \cdot 2H_2O$ (2.5 mM, 40 mL) was added drop by drop into the above solution. After continually stirring for 4 h in the dark, the obtained yellow precipitate of Ag_2MoO_4–WO_3 was separated by centrifugation with deionized water and ethanol for several times and dried at 30 °C for 6 h in vacuum drier. For comparison, pure Ag_2MoO_4 was also prepared with this method without WO_3.

2.4. Characterization

Scanning Electron Microscopy (SEM) and Transmittance Electron Microscopy (TEM) were performed on field emission scanning electron microscope (Hitachi S-4800) and field emission electron microscope (FEI TECNAI G2 F20 200 kV) to reveal the morphology of the catalysts. Powder X-ray diffractometer (XRD) patterns were recorded on Bruker D8 ADVANCE to analysis the phases of the catalysts. UV-vis diffuse reflectance spectra (DRS) were recorded on a UV-vis spectrophotometer (Shimadzu Corporation, UV-3600), and the specific surface area (BET) measurements were performed on a N_2 adsorption specific surface & pore size analysis instrument (3H-2000PS1, Beishide Instrument S&T). Photoluminescence (PL) spectra were measured on the F-7000, Hitachi spectrophotometer at room temperature, and the wavelength of excitation light was 325 nm.

2.5. Photocatalytic test

The photocatalytic performances were evaluated with the photodegradation of RhB, 4-CP and TC under visible-light irradiation (300 W Xe lamp with a cut-off filter, $\lambda > 420$ nm). The photo of the reaction setting up was shown in Fig. S1.† In each typical experiment, 100 mg catalyst was added into 100 mL RhB, 4-CP or TC solution (10 mg L^{-1}). To establish the adsorption–desorption equilibrium between the catalysts and the pollutants, the suspension was magnetically stirred in dark for 60 min before the light irradiation. During irradiation, 2.0 mL suspension was collected at the regular intervals and centrifuged to remove the catalysts in RhB solution or filtered through a Navigator syringe filter of 0.22 μm in TC and 4-CP solution. The concentrations of RhB were determined by UV-6000PC spectrophotometer at the characteristic absorption peak of RhB (553 nm), and the concentrations of 4-CP and TC were recorded with the high-performance liquid chromatography (HPLC, Agilent 1100 series) equipped with a UV detector at 280 nm. The flow rate of mobile phase (TC: 8% methanol, 72% oxalic acid and 20% acetonitrile; 4-CP: 80% methanol and 20% water) was set at 0.5 mL min^{-1}.

To determine the free radical in the progress of photodegradation, 6 mM $AgNO_3$, 1 mM disodium ethylene diamine tetraacetate (Na_2-EDTA), 1 mM *p*-benzoquinone (BQ) or 1 mM isopropanol (IPA) were employed as sacrifice agents in the RhB (100 mL, 10 mg L^{-1}) photocatalytic process.

2.6. Photoelectrochemical measurements

The photoelectrochemical measurements were conducted on a CHI660E electrochemical workstation using a standard three-electrode system in which a saturated calomel electrode (SCE), a platinum sheet (2 cm^2) and a FTO glass (2 cm^2) coated with Ag_2MoO_4, WO_3 and 10% Ag–W film were used as reference, counter and working electrodes, respectively. While 0.5 M Na_2SO_4 solution was used as the electrolyte. In addition, the potential of the EIS measurements was the open-circuit potential. The photocurrent responses of the samples were determined under inconsecutive irradiation by 300 W Xe lamp. During the experiment, the test potential was 0.5 V *vs.* SCE.

3. Results and discussion

3.1. Preparation of Ag_2MoO_4/WO_3 heterojunctions

A series of Ag_2MoO_4/WO_3 heterojunctions were prepared by a facile precipitation–deposition method, as shown in Fig. 1. Firstly, WO_3 plates were synthesized by the reaction of $Na_2WO_4 \cdot 2H_2O$ and HCl during the hydrothermal treatment. Subsequently, Ag_2MoO_4 NPs were *in situ* anchored onto the plate-like WO_3 substrate by the reaction of Na_2MoO_4 and $AgNO_3$ at room temperature. The

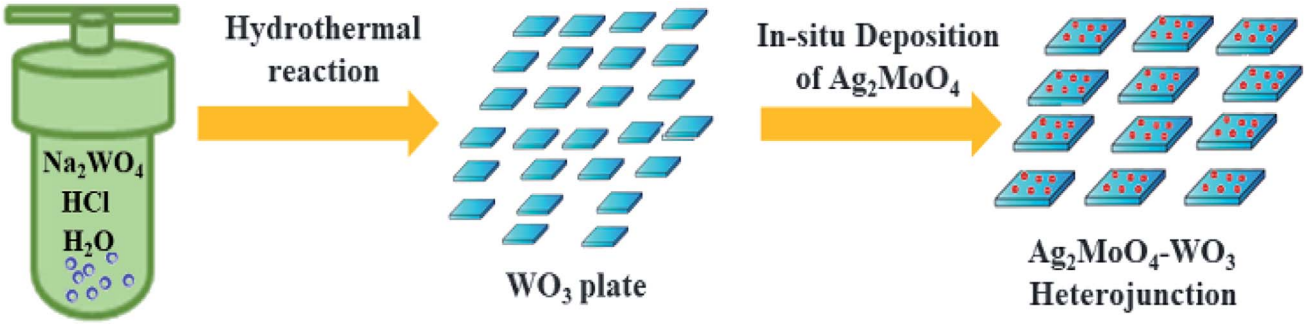

Fig. 1 Schematic illustration for the preparation of Ag_2MoO_4/WO_3 heterojunction.

resulting catalysts with different Ag_2MoO_4 weight percentage of 5, 10, 15 and 20% are abbreviated as 5, 10, 15, and 20% Ag–W respectively.

3.2. Characterization of photocatalysts

The morphology of WO_3 and Ag–W heterojunctions have also been characterized by SEM. As shown in Fig. 2A and B, the WO_3 displays a uniform nanoplate morphology, with an average length of 150–200 nm, which can also be further demonstrated by the TEM image (Fig. 2C) and the HRTEM (Fig. 2D) which showed the facet (200) is the dominating facet. After the surface decoration with Ag_2MoO_4, the obtained Ag–W heterojunction retain the nanoplate morphology (Fig. 3A). Notably, TEM images of Ag–W heterojunctions shows that there are plenty of small Ag_2MoO_4 nanoparticles distributed on WO_3 nanoplates (Fig. 3B and C). In addition, the high-resolution TEM (HRTEM) image (Fig. 3D) clearly displays two sets of lattice fringes with inter-plane spacings of 0.364 nm and 0.233 nm, which can be well assigned to the values for the (200) crystal plane of monoclinic WO_3 (JCPDS card no. 43-1035) and the (400) crystal plane of cubic Ag_2MoO_4 (JCPDS card no. 08-0473), respectively. Furthermore, the EDS pattern (Fig. 4A) reveals that Ag–W heterojunctions were composed of W, Ag, O and Mo elements. The molar ratio of W to Mo is 73 : 2.1, suggesting that the weight ratio of Ag_2MoO_4 to WO_3 species is equal to 0.09 : 1. The above results confirm the formation of Ag–W heterojunctions.

The crystal phases of all as-prepared photocatalysts were tested by the XRD to demonstrate the phase and crystallinity (Fig. 4B). The standard XRD pattern of Ag_2MoO_4 and WO_3 have also been supplied. All the diffraction peaks of pure WO_3 can be well indexed to monoclinic WO_3 (JCPDS card no. 43-1035), while all diffraction peaks of pure Ag_2MoO_4 can be well assigned to cubic Ag_2MoO_4 (JCPDS card no. 08-0473). For Ag–W heterojunctions, they showed the co-existence of Ag_2MoO_4 and WO_3.

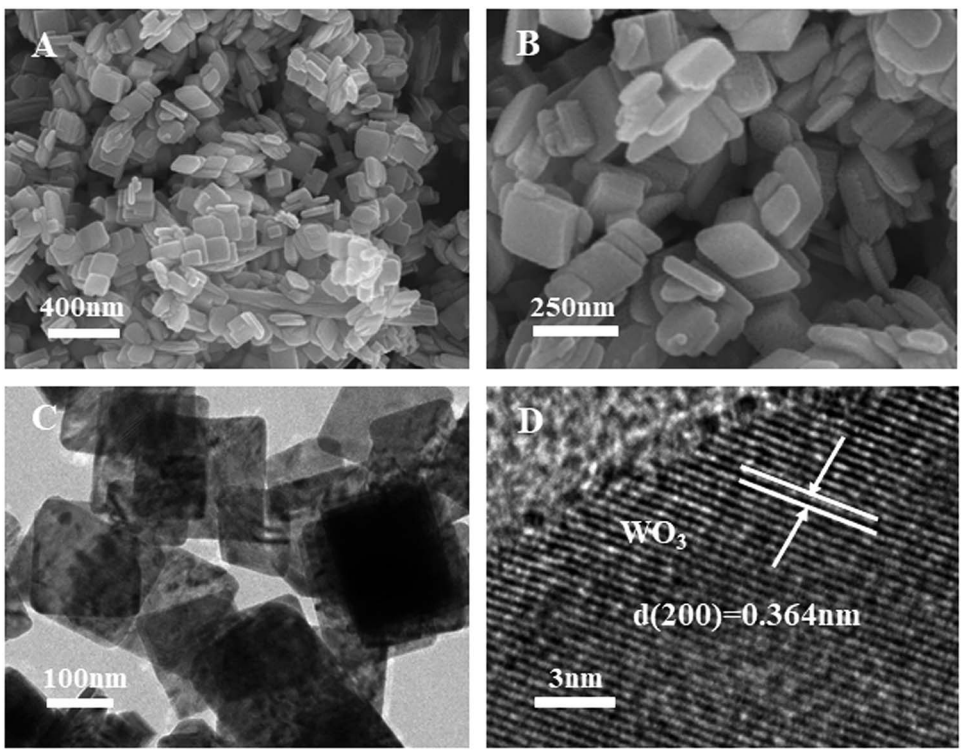

Fig. 2 (A) SEM, (B) enlarged SEM of WO_3 nanoplates, (C) TEM image and (D) HRTEM images of WO_3 nanoplates with dominating 200 facets.

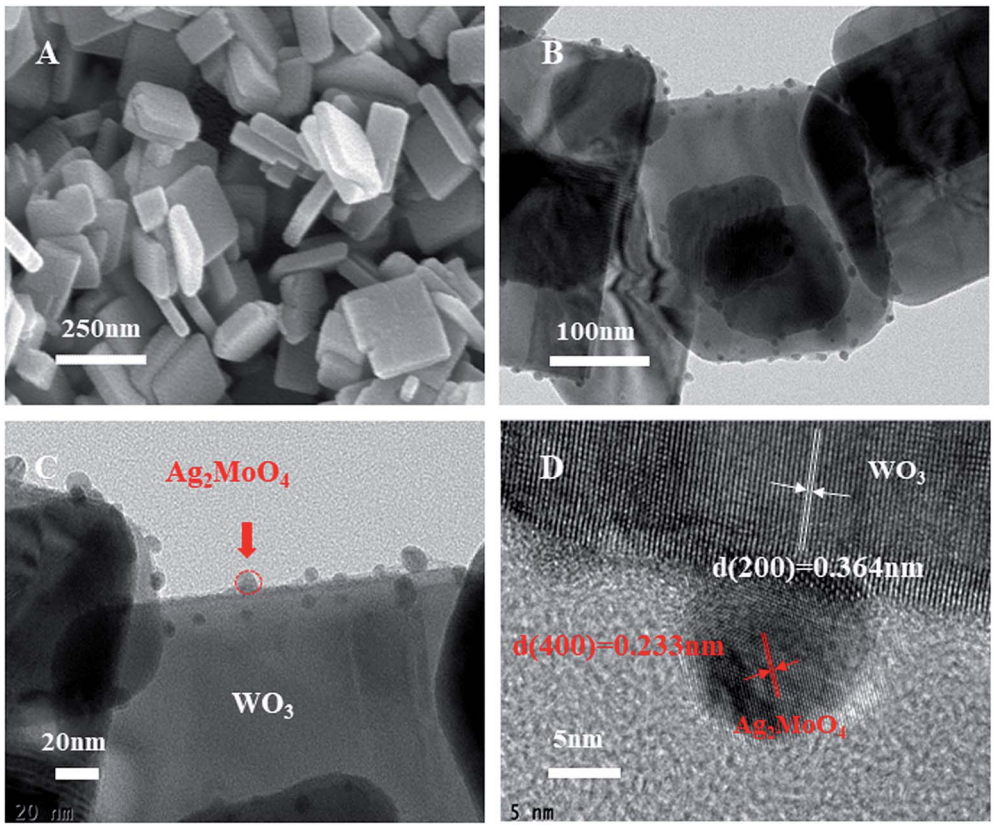

Fig. 3 (A) SEM, (B and C) TEM, and (D) HRTEM images of 10% Ag–W heterojunction: Ag_2MoO_4 nanoparticles were selectively deposited on 200 facets.

Major diffraction peaks with 2θ values of 23.1°, 23.6°, 24.4°, 26.6°, 28.9°, 34.2° and 49.9° could be perfectly indexed to the (002), (020), (200), (120), (112), (202) and (140) crystal planes of monoclinic WO_3 (JCPDS card no. 43-1035), respectively. Besides, additional diffraction peaks with 2θ values of 27.1°, 31.8°, 33.3°, 38.6°, 50.9° and 55.8° could be attributed to the (220), (311), (222), (400), (511) and (440) crystal planes of cubic Ag_2MoO_4 (JCPDS card no. 08-0473), respectively.

The UV-vis diffuse reflectance spectra of pure Ag_2MoO_4, WO_3 and 10% Ag–W heterojunction have been recorded in order to investigate the capacity of visible light absorption, as shown in Fig. 5A. Clearly, pure Ag_2MoO_4 shows a typical absorption at wavelength shorter than 400 nm, which accords previous reports.[35] Pure WO_3 exhibits an obviously absorption edge at *ca.* 500 nm, consistent with the previous reports.[31] Interestingly, 10% Ag–W heterojunction displays a broad-spectrum photo absorption with an edge at *ca.* 530 nm, reflecting a red shift of photo absorption. This red shift of photoabsorption maybe resulting from the partial interfacial charge transfer between Ag_2MoO_4 and WO_3 which is caused by the staggered bandgap.[11] Therefore, VLD photocatalytic activity of 10% Ag–W heterojunction can be expected to be superior to that of Ag_2MoO_4 and WO_3.

The E_g (energy band gaps) of Ag_2MoO_4 and WO_3 can be estimated from a linear transformation $(h\nu)$–$(Ah\nu)^2$ curves, as Fig. 5B presents. Accordingly, E_g of Ag_2MoO_4 and WO_3 are calculated to be 3.38 and 2.54 eV, severally. In addition, the positions of the valence band (VB) and conduction band (CB) of photocatalysts have also been figured out by Mulliken electronegativity:[35]

$$E_{CB} = X - E_C - 1/2E_g \quad (1)$$

$$E_{VB} = E_{CB} + E_g \quad (2)$$

Here, X is the absolute electronegativity of the corresponding semiconductors (Ag_2MoO_4 and WO_3), E_C is the energy of free electrons on the hydrogen scale (4.5 eV). According to the above equations, the E_{CB} and E_{VB} of Ag_2MoO_4 were calculated to be −0.28 and 3.1 eV, while those of WO_3 were calculated to be 0.82 and 3.36 eV, respectively.

The N_2 isothermal adsorption desorption curves of WO_3, Ag_2MoO_4 and 10% Ag–W heterostructures have also been recorded. As shown in Fig. 6, WO_3 and 10% Ag–W heterostructure exhibit a similar BET surface area of about 12 $m^2\ g^{-1}$. In addition, according to the desorption branches in the inset of Fig. 6, the pore size distribution presents nanopores (~26.5 nm) in 10% Ag–W heterostructure, which is usually benefit for the improvement of the photocatalytic activity.

3.3. Photocatalytic activity

The photocatalytic activities of Ag–W heterostructures with different weight ration of Ag_2MoO_4 and WO_3 were evaluated by

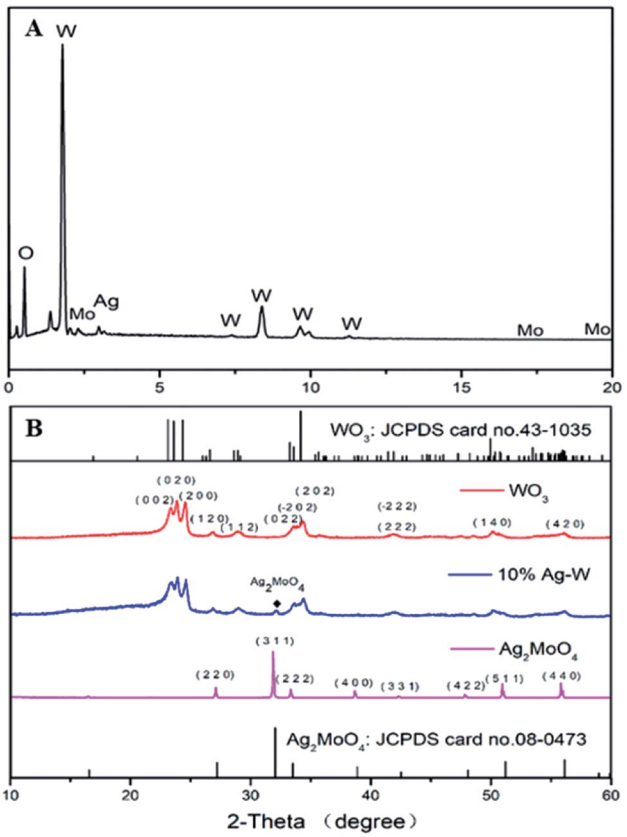

Fig. 4 (A) EDS of 10% Ag–W heterojunction; (B) XRD patterns of as-prepared 10% Ag–W heterojunction compared with JCPDS of Ag_2MoO_4 and WO_3.

the photodegradation of dye RhB, colorless 4-CP and antibiotic TC under visible light irradiation at room temperature. For comparison, pure WO_3, Ag_2MoO_4 and P25 have also been used as photocatalysts.

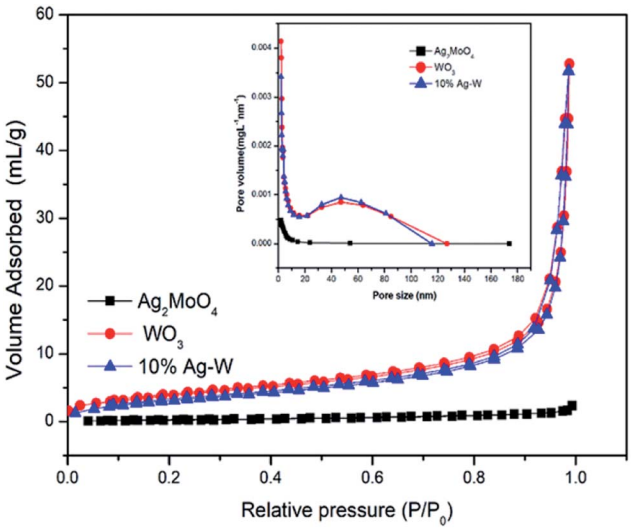

Fig. 6 N_2 adsorption–desorption isotherms and the corresponding pore size distribution (inset) of WO_3, Ag_2MoO_4 and 10% Ag–W heterojunction.

Fig. 7A presents the photodegradation efficiency of RhB over different photocatalysts. Clearly, all the Ag–W heterostructures (5% Ag–W, 10% Ag–W, 15% Ag–W and 20% Ag–W) exhibited remarkable enhanced photocatalytic performance in comparison with bare WO_3 and Ag_2MoO_4, and the RhB photodegradation efficiencies reached up to 95%, 97%, 89% and 73%, respectively within 160 min of reaction. Among these photocatalysts, 10% Ag–W heterostructures showed the most excellent photocatalytic performance, it's photocatalytic activity was more than 2 and 1.9 times than that of Ag_2MoO_4 and WO_3 respectively. In addition, the photodegradation efficiency of TC and 4-CP over Ag–W heterostructures with different Ag_2MoO_4

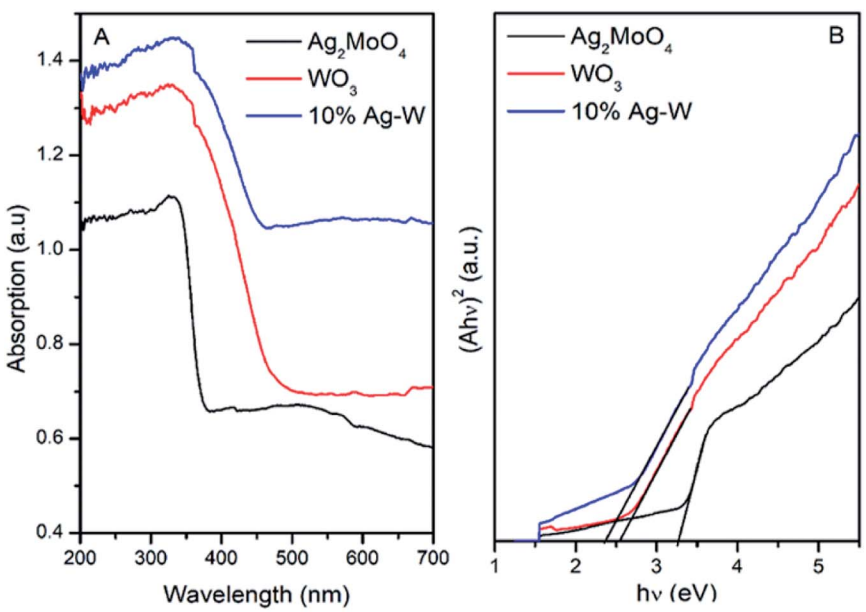

Fig. 5 UV-vis diffuse reflectance spectra (A) and linear transformation $(h\nu)$–$(Ah\nu)^2$ curves (B) of Ag_2MoO_4, WO_3 and 10% Ag–W heterojunction.

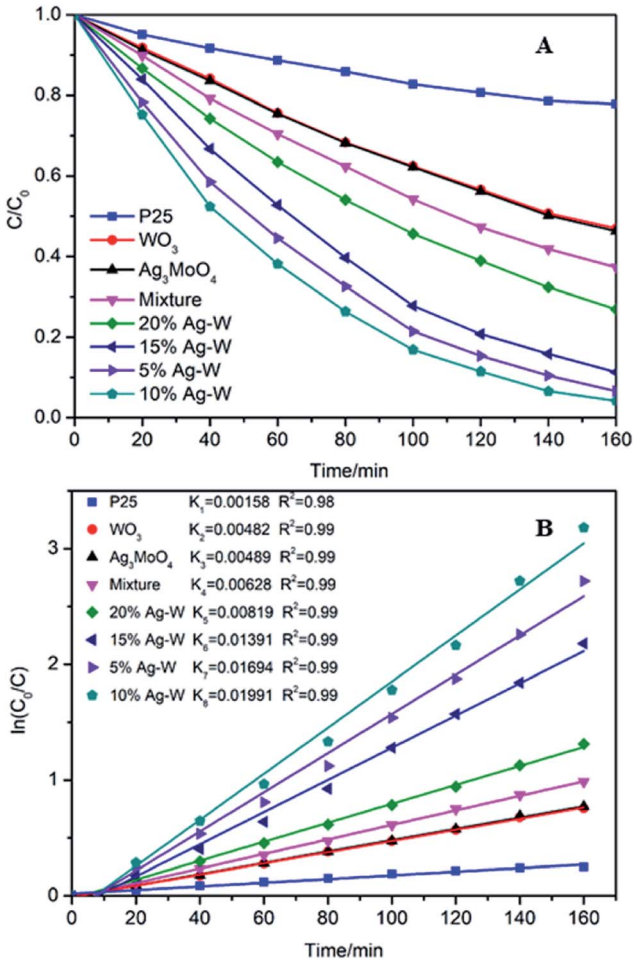

Fig. 7 Degradation curves (A) and (B) rate constants (k) under the visible light irradiation (λ > 420 nm) over different photocatalysts.

content have also been investigated respectively, 10% Ag–W heterostructures also showed the most excellent photocatalytic performance (Fig. S2 and S3†). Moreover, the load content of Ag_2MoO_4 had a prominent effect on the photocatalytic performance, too low or high content of Ag_2MoO_4 loading could not improve the separation of charges effectively, leading to an unsatisfactory photocatalytic performance. Similar results have also been observed by previous reports.[31,43,44] Furthermore, the photodegradation efficiency of 10% Ag–W (97%) was almost 3.88 times higher than that of P25.

Moreover, the degradation efficiency were further analyzed by using the pseudofirst-order model,[45] $-\ln(C/C_0) = kt$. In this formula, C_0 represents the initial concentration of RhB, C represents the concentration of RhB at time t, and k represents the reaction rate constant. As shown in Fig. 7B, clearly, 10% Ag–W exhibited the highest k value (0.01991 min^{-1}), which was extremely higher than those of Ag_2MoO_4 (0.00482 min^{-1}) and WO_3 (0.00489 min^{-1}), and is more than 10 times that of TiO_2 (0.00158 min^{-1}). In addition, to further confirm the effect of the heterojunctions in Ag–W heterojunction, the degradation of RhB by using the mixture of two single components of Ag–W heterostructures with the same weights (90 mg WO_3 + 10 mg Ag_2MoO_4) as photocatalysts have also been conducted under visible light irradiation. The photodegradation efficiency over 10% Ag–W was almost 1.43 times than that of the mechanical mixture of WO_3 and Ag_2MoO_4 (68%), and the k over 10% Ag–W was more than 3 times than that of the mixture (0.00628 min^{-1}). All of these results demonstrated that there was a synergic effect between the two components (WO_3 and Ag_2MoO_4) in Ag–W heterostructures.

To preclude the dye sensitization effect during the photocatalytic degradation, colorless antibiotic TC and 4-CP have also been chosen as model pollutants. As shown in the illustrated HPLC chromatograms of TC and 4-CP solution at the regular intervals times (Fig. 8A). When TC was chosen as model pollutants, the characteristic peak of TC solution at retention time (5.8 min) decreased quickly (Fig. 8A). After 210 minutes irradiation, the degradation efficiency of TC reached up to 99%. Similar with the result of the HPLC chromatograms of 4-CP solution, the degradation efficiency of 4-CP reached up to 70% within 320 minutes (Fig. 8B), demonstrating the remarkable photodegradation of 10% Ag–W heterojunction.

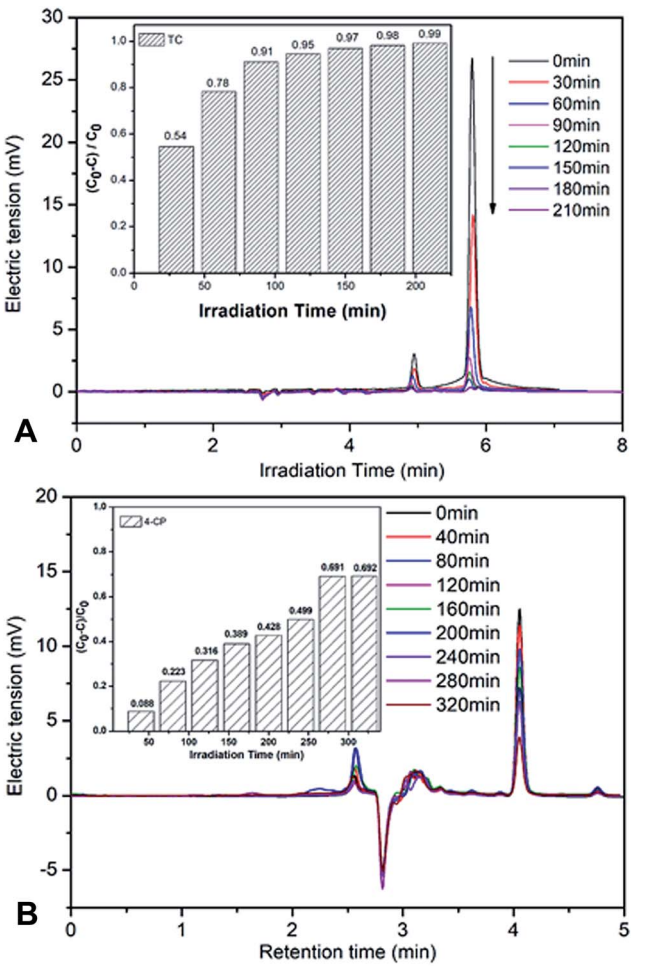

Fig. 8 HPLC chromatograms of (A) TC (100 mL 5 mg L^{-1}) and (B) 4-CP (100 mL 5 mg L^{-1}) solutions over the 10% Ag–W heterojunction for different photocatalytic reaction times, inset: the photodegradation efficient column of (A) TC and (B) 4-CP under visible light irradiation (λ > 420 nm).

The stability of photocatalysts is one of most significant factors in practical applications. Hence, the photocatalytic stability of the 10% Ag–W heterojunction was researched by repeatability experiments for photodegradation of RhB under visible-light irradiation (Fig. 9A). After four consecutive runs, the photodegradation efficiency of 10% Ag–W heterojunction maintains 93%, and the k decrease slightly from 0.01991 min^{-1} to 0.01679 min^{-1} (Fig. S4†). The slight decrease of its activity should result from the loss of samples in the recycle experiments. All these results demonstrate the excellent recyclability of Ag–W heterojunction.

3.4. Photocatalytic photodegradation mechanism

During the photocatalysis process, the photogenerated electrons (e^-) and holes (h^+) can transfer to the surface of catalyst and will generate sorts of reactive species, such as hydroxyl radicals ($\cdot OH$), superoxide radicals ($\cdot O_2^-$) and so on, which play an important role in photodegrading organic contaminant.[46–48] Herein, we evaluated the dominating active species during the process of photodegradation of RhB. In the photodegradation experiments, $AgNO_3$, disodium ethylene diamine tetraacetate (Na_2-EDTA), benzoquinone (BQ) and isopropanol (IPA) which acted as the scavengers of e−, h^+, $\cdot O_2^-$, $\cdot OH$[38,49] were added into RhB suspensions before visible light irradiation respectively. Just as shown in Fig. 9B, when Na_2-EDTA and IPA were added into the RhB solution, the photocatalytic efficiency decreases sharply, the k value decrease to less than 1/10 of the original one (Fig. S5†), and the RhB degradation efficiency decreases from 94.9% to 50% or 19.3% respectively after 160 min of reaction. While the photocatalytic activities are influenced slightly with the addition of $AgNO_3$ and BQ. These results illustrate that h^+

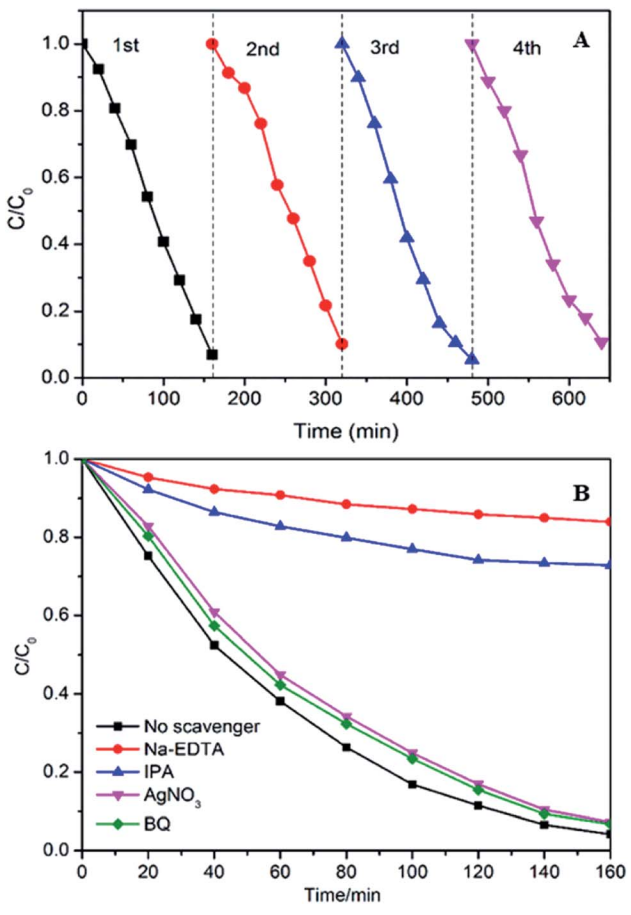

Fig. 9 (A) Cycling runs in photocatalytic photodegradation of RhB (10 mg L^{-1}, 100 mL) over 10% Ag–W heterojunction (100 mg) under visible light (λ > 420 nm); (B) effect of different scavengers on the degradation of RhB (10 mg L^{-1}, 100 mL) efficiencies over 10% Ag–W heterojunction.

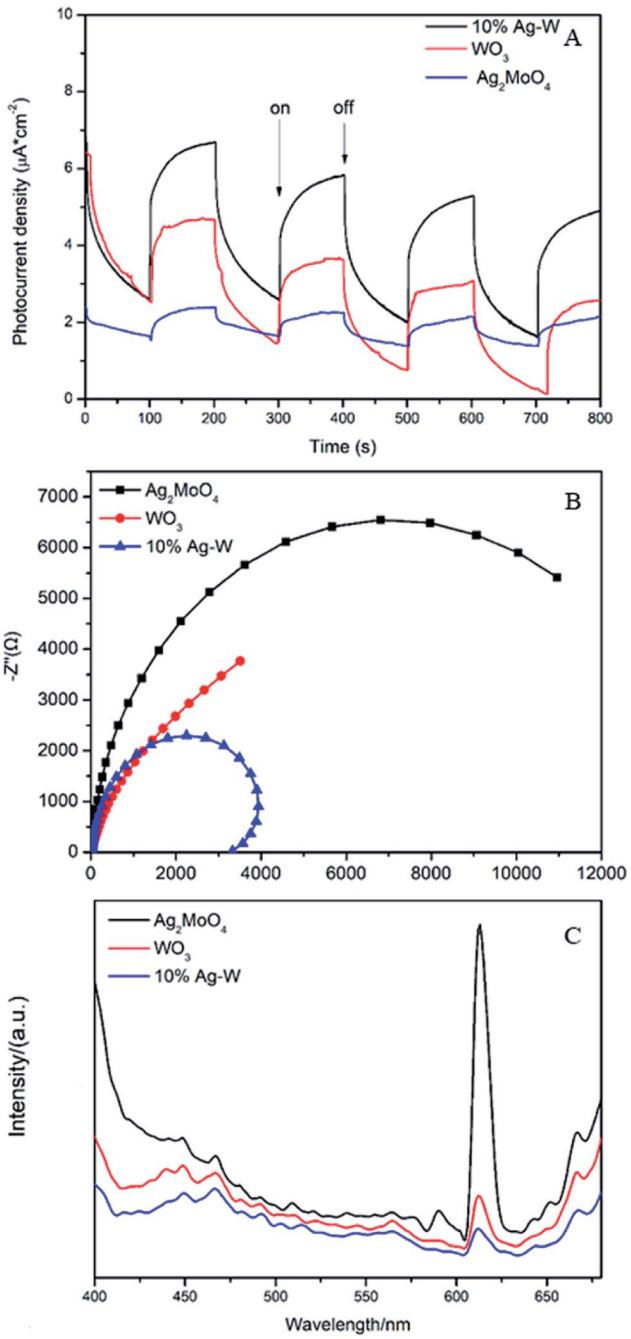

Fig. 10 Photocurrent density (A), EIS plots (B) and PL plots (C) of WO_3, Ag_2MoO_4 and 10% Ag–W heterojunction.

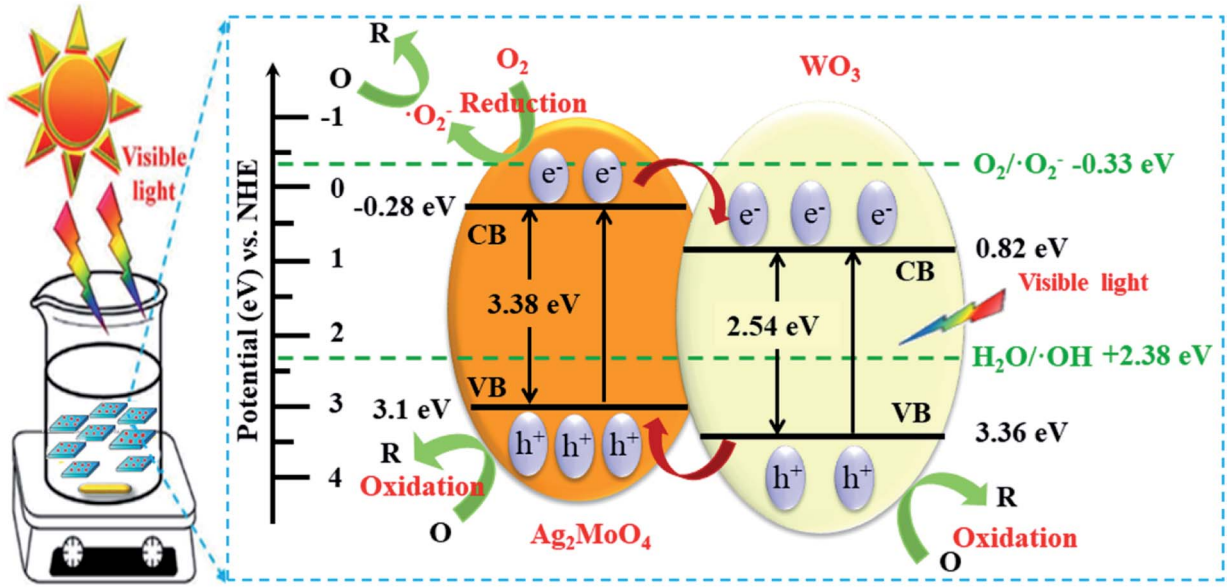

Fig. 11 Schematic diagrams of electron–hole pair separation and the possible photodegradation mechanism over Ag–W heterojunction under visible-light irradiation.

and ·OH are the primary active species which conduce to the photodegradation of RhB.

To investigate the electronic interaction between Ag_2MoO_4 and WO_3, the photocurrents of 10% Ag–W heterojunction, Ag_2MoO_4 and WO_3 electrodes have also been measured. To the best of our knowledge, the intensity of photocurrent reflects the transference speed of photogenerated electrons and holes. Clearly, all the electrodes showed fast and uniform photocurrent responses in Fig. 10A. Under visible light irradiation, the intensity photocurrent of 10% Ag–W heterojunction was almost 6 and 2 times than that of Ag_2MoO_4 and WO_3, respectively (Fig. 10A). The photocurrent enhancement of 10% Ag–W heterojunction manifested that Ag–W heterojunction can efficiently accelerate the separation of photogenerated electrons and holes due to the synergetic effect of Ag_2MoO_4 and WO_3 semiconductor. In addition, EIS analysis has also been measured to further study the electron transport property of the 10% Ag–W heterojunction, Ag_2MoO_4 and WO_3 electrodes. Usually, a smaller circular radius in EIS Nyquist plot represents a lower charge transfer resistance in the electrode.[50] Obviously, the EIS Nyquist plot of 10% Ag–W heterojunction showed the smallest circular radius among the three electrodes (Fig. 10B), suggesting the lowest charge transfer resistance. To further confirm the charge transfer property, the PL emission spectrum which can be used to evaluate the separation efficiency of photogenerated electron–hole pairs was employed (Fig. 10C). Generally, a weaker intensity of the PL emission spectra represents a lower charge recombination rate.[51] As shown in Fig. 10C, 10% Ag–W heterojunction display the lowest intensity under the excitation of light at $\lambda = 325$ nm, further indicating the vital role in the suppression of the recombination of photogenerated charge carriers.

Based on the above results, the possible photodegradation mechanism for the enhanced photocatalytic activity of Ag–W heterojunction are analyzed. Two main reasons contributing to the improved photocatalytic performance of Ag–W heterojunction. On one hand, the improvement of the photoabsorption of visible-light enhances the utilization of solar energy and hence product more photogenerated holes and electrons, as shown in Fig. 11. On the other hand, the staggered bandgap and intimate contact between Ag_2MoO_4 and WO_3 greatly promote the charge separation and transfer in the Ag–W heterojunction.[52–59] Under visible light irradiation, both Ag_2MoO_4 and WO_3 can be excited to photogenerated electron–hole pairs. Since the potentials for CB and VB of Ag_2MoO_4 are more negative than that of Ag_2MoO_4, photogenerated electrons in the CB of Ag_2MoO_4 can be transferred to that of WO_3 while holes in the VB of WO_3 can be transferred to that of Ag_2MoO_4. Therefore, such charge transfer process can suppress the recombination of electron–hole pairs effectively, which has also been confirmed by the photocurrent measurements, EIS and PL emission spectrum. Consequently, numerous h^+ accumulated on the VB of Ag_2MoO_4 can directly oxidize organic contaminant adsorbed on the surface of the photocatalyst or mineralized them indirectly through hydroxyl radicals (·OH) generated by the reaction of holes and H_2O or OH^-.

4. Conclusions

In summary, we designed and prepared a novel the Ag–W heterojunction with different mass percentage though a facile precipitation method. These heterogeneous photocatalysts showed extremely superior photocatalytic performance than bare Ag_2MoO_4 and WO_3 for RhB/4-CP/TC photodegradation, and the 10% Ag–W exhibits the most excellent photocatalytic activity. Moreover, the mechanism of the enhanced photocatalytic activity of Ag–W heterojunctions has been analyzed based on the energy band positions and the free radical capture experiments. The enhancement of the photocatalytic

performance is mainly attributed to the stagger band gap structure, improved the separation of photogenerated electron–hole pairs. Furthermore, the Ag–W heterojunction exhibits good stability with inappreciable loss after four cycling runs. Therefore, this work may provide new insight for developing VLD photocatalyst on application of environmental renovation.

Conflicts of interest

There are no conflicts to declare.

Acknowledgements

This work has been financially supported by the Qingdao Science and Technology Program (16-5-1-32-jch, 17-3-3-77-nsh), the China Postdoctoral Science Foundation (2016M602110), the National Natural Science Foundation of China (31570541, 31170509, 21506109), the Key R&D project of Shandong province (GG201809130031) and the Primary Research and Development Plan of Shandong Province (2017GSF220001).

Notes and references

1 A. Kudo and Y. Miseki, *Chem. Soc. Rev.*, 2009, **38**, 253–278.
2 J. Liu, Y. Liu, N. Liu, Y. Han, X. Zhang, H. Huang, Y. Lifshitz, S.-T. Lee, J. Zhong and Z. Kang, *Science*, 2015, **347**, 970–974.
3 X. Chen and C. Burda, *J. Am. Chem. Soc.*, 2008, **130**, 5018–5019.
4 X. Chen and S. S. Mao, *J. Nanosci. Nanotechnol.*, 2006, **6**, 906–925.
5 Y. Bi, S. Ouyang, N. Umezawa, J. Cao and J. Ye, *J. Am. Chem. Soc.*, 2011, **133**, 6490–6492.
6 R. Qu, W. Zhang, N. Liu, Q. Zhang, Y. Liu, X. Li, Y. Wei and L. Feng, *ACS Sustainable Chem. Eng.*, 2018, **6**, 8019–8028.
7 Y. Wang, H. Wang, A. Xu and Z. Song, *J. Mater. Sci.: Mater. Electron.*, 2018, **29**, 16691–16701.
8 H. Fu, C. Pan, W. Yao and Y. Zhu, *J. Phys. Chem. B*, 2005, **109**, 22432–22439.
9 C. Zhang and Y. Zhu, *Chem. Mater.*, 2005, **17**, 3537–3545.
10 L. Zhang, H. Wang, Z. Chen, P. K. Wong and J. Liu, *Appl. Catal., B*, 2011, **106**, 1–13.
11 H. Wang, S. Li, L. Zhang, Z. Chen, J. Hu, R. Zou, K. Xu, G. Song, H. Zhao and J. Yang, *CrystEngComm*, 2013, **15**, 9011–9019.
12 Y. Li, H. Wang, L. Xie, Y. Liang, G. Hong and H. Dai, *J. Am. Chem. Soc.*, 2011, **133**, 7296–7299.
13 B. Hinnemann, P. G. Moses, J. Bonde, K. P. Jørgensen, J. H. Nielsen, S. Horch, I. Chorkendorff and J. K. Nørskov, *J. Am. Chem. Soc.*, 2005, **127**, 5308–5309.
14 S. Yan, Z. Li and Z. Zou, *Langmuir*, 2009, **25**, 10397–10401.
15 W.-J. Ong, L.-L. Tan, Y. H. Ng, S.-T. Yong and S.-P. Chai, *Chem. Rev.*, 2016, **116**, 7159–7329.
16 T. W. Kim and K.-S. Choi, *Science*, 2014, **343**, 990–994.
17 D. Chen and J. Ye, *Adv. Funct. Mater.*, 2008, **18**, 1922–1928.
18 J. Su, L. Guo, N. Bao and C. A. Grimes, *Nano Lett.*, 2011, **11**, 1928–1933.
19 P. M. Rao, L. Cai, C. Liu, I. S. Cho, C. H. Lee, J. M. Weisse, P. Yang and X. Zheng, *Nano Lett.*, 2014, **14**, 1099–1105.
20 S. Chen, Y. Hu, S. Meng and X. Fu, *Appl. Catal., B*, 2014, **150**, 564–573.
21 B. Roose, K. C. Gödel, S. Pathak, A. Sadhanala, J. P. C. Baena, B. D. Wilts, H. J. Snaith, U. Wiesner, M. Grätzel and U. Steiner, *Adv. Energy Mater.*, 2016, **6**, 1501868.
22 H. Wang, L. Zhang, Z. Chen, J. Hu, S. Li, Z. Wang, J. Liu and X. Wang, *Chem. Soc. Rev.*, 2014, **43**, 5234–5244.
23 S. Xu, H. Lu, L. Chen and X. J. R. A. Wang, *RSC Adv.*, 2014, **4**, 45266–45274.
24 J. Low, J. Yu, M. Jaroniec, S. Wageh and A. Al-Ghamdi, *Adv. Mater.*, 2017, **29**, 1601694.
25 T. Zhang, M. Liu, Y. Meng, B. Huang, X. Pu and X. Shao, *Sep. Purif. Technol.*, 2018, **206**, 149–157.
26 G. Wu, J. Ma, S. Li, J. Guan, B. Jiang, L. Wang, J. Li, X. Wang and L. Chen, *J. Colloid. Interf. Sci.*, 2018, **528**, 360–371.
27 J. Fu, Q. Xu, J. Low, C. Jiang and J. Yu, *Appl. Catal., B*, 2019, **243**, 556–565.
28 J. Zhang and Z. J. R. A. Ma, *RSC Adv.*, 2017, **7**, 2163–2171.
29 J. Jin, J. Yu, D. Guo, C. Cui and W. Ho, *Small*, 2015, **11**, 5262–5271.
30 W. Zhu, J. Liu, S. Yu, Y. Zhou and X. Yan, *J. Hazard. Mater.*, 2016, **318**, 407–416.
31 W. Zhu, F. Sun, R. Goei and Y. Zhou, *Appl. Catal., B*, 2017, **207**, 93–102.
32 L. Tian, L. Ye, J. Liu and L. Zan, *Catal. Commun.*, 2012, **17**, 99–103.
33 Y.-Y. Bai, Y. Lu and J.-K. Liu, *J. Hazard. Mater.*, 2016, **307**, 26–35.
34 Z. Wang, J. Zhang, J. Lv, K. Dai and C. Liang, *Appl. Surf. Sci.*, 2017, **396**, 791–798.
35 A. Esfandiar, A. Irajizad, O. Akhavan, S. Ghasemi and M. R. Gholami, *Int. J. Hydrogen Energy*, 2014, **39**, 8169–8179.
36 M. Pandiri, R. Velchuri, R. Gundeboina and V. Muga, *J. Photochem. Photobiol., A*, 2018, **360**, 231–241.
37 Z. Jiao, J. Zhang, Z. Liu and Z. Ma, *J. Photochem. Photobiol., A*, 2019, **371**, 67–75.
38 W. Cao, Y. An, L. Chen and Z. Qi, *J. Alloys Compd.*, 2017, **701**, 350–357.
39 Y. Bai, Y. Lu and J. Liu, *J. Hazard. Mater.*, 2016, **307**, 26–35.
40 Y.-Y. Bai, Y. Lu and J.-K. Liu, *J. Hazard. Mater.*, 2016, **307**, 26–35.
41 Z. Wang, J. Lv, J. Zhang, K. Dai and C. Liang, *Appl. Surf. Sci.*, 2018, **430**, 595–602.
42 W. Cao, Y. An, L. Chen and Z. Qi, *J. Alloys Compd.*, 2017, **701**, 350–357.
43 R. Dhanabal, S. Velmathi and A. C. Bose, *Catal. Sci. Technol.*, 2016, **6**, 8449–8463.
44 W. Liu, J. Shen, X. Yang, Q. Liu and H. Tang, *Appl. Surf. Sci.*, 2018, **456**, 369–378.
45 X.-j. Wang, Q. Wang, F.-t. Li, W.-y. Yang, Y. Zhao, Y.-j. Hao and S.-j. Liu, *Chem. Eng. J.*, 2013, **234**, 361–371.
46 L. Ge, C. Han and J. Liu, *Appl. Catal., B*, 2011, **108**, 100–107.
47 L. Cai, H. Jiang and L. Wang, *Appl. Surf. Sci.*, 2017, **420**, 43–52.

48 J. Lin, Y. Liu, Y. Liu, C. Huang, W. Liu, X. Mi, D. Fan, F. Fan, H. Lu and X. Chen, *ChemSusChem*, 2019, **12**, 961–967.
49 N. Shao, J. Wang, D. Wang and P. Corvini, *Appl. Catal., B*, 2017, **203**, 964–978.
50 J. Yang, W. Li, J. Li, D. Sun and Q. Chen, *J. Mater. Chem.*, 2012, **22**, 17744–17752.
51 Y. Hao, X. Dong, S. Zhai, X. Wang, H. Ma and X. Zhang, *Chem. Commun.*, 2016, **52**, 6525–6528.
52 M. Green, Z. Liu, P. Xiang, Y. Liu, M. Zhou, X. Tan, F. Huang, L. Liu and X. Chen, *Light: Sci. Appl.*, 2018, **7**, 87.
53 L. Guan and X. Chen, *ACS Appl. Energy Mater.*, 2018, **1**, 4313–4320.
54 R. Shen, J. Xie, P. Guo, L. Chen, X. Chen and X. Li, *ACS Appl. Energy Mater.*, 2018, **1**, 2232–2241.
55 X. Chen, F. Liu, X. Yan, Y. Yang, Q. Chen, J. Wan, L. Tian, Q. Xia and X. Chen, *Chem.–Eur. J.*, 2015, **21**, 18711–18716.
56 F. Liu, X. Chen, Q. Xia, L. Tian and X. Chen, *RSC Adv.*, 2015, **5**, 77423–77428.
57 J. Gao, B. Jiang, C. Ni, Y. Qi and X. Bi, *Chem. Eng. J.*, DOI: 10.1016/j.cej.2019.123034.
58 Y. Zhang, L. Luo, Z. Shi, X. Shen, C. Peng, J. Liu, Z. Chen, Q. Chen and L. J. C. Zhang, *ChemCatChem*, 2019, **11**, 2855–2863.
59 Y. Liu, X. Mi, J. Wang, M. Li, D. Fan, H. Lu and X. Chen, *Inorg. Chem. Front.*, 2019, **6**, 948–954.